METHODS

Melt Pool Width Extraction Method in Laser Directed Energy Deposition Based on Variable Step Size Erosion Model

YUANXIN CHAI[1], LIGUO MIAO[1], JINGHU TANG[2], AND DIANQI LI[1]
[1]School of Mechanical Engineering, Shenyang University of Technology, Shenyang 110870, China
[2]School of Mechanical Engineering and Automation, Northeastern University, Shenyang 110819, China

Corresponding author: Liguo Miao (18842553012@163.com)

ABSTRACT To solve the problem of insufficient melt pool width feature extraction accuracy caused by splash, arc light, and other interferences in the metal deposition process, a melt pool width extraction method based on the variable step size erosion model is proposed according to the characteristics of the spatial distribution of the melt pool size features. To achieve accurate measurement of the melt pool width, the melt pool image is first denoised using mathematical morphology and then segmented roughly using manual thresholding. Subsequently, the melt pool contour is iterated using an erosion model to obtain precise point localization information after fine segmentation, followed by the calculation of the melt pool width. Comparison experiments demonstrate that the method exhibits excellent accuracy and robustness in extracting melt pool width, while also showcasing high efficiency in fulfilling the requirements for closed-loop control. These findings lay the groundwork for the closed-loop control of the melt pool size.

INDEX TERMS Laser metal deposition, melt pool width, erosion modeling, feature extraction.

I. INTRODUCTION

Laser cladding is commonly employed in surface repair and strengthening applications owing to its high precision and efficiency [1], [2], [3]. However, the quality of cladding can be compromised by variations in environmental conditions [4], [5]. The melt pool, the smallest unit formed during the laser cladding process, plays a crucial role in determining the stability of the deposition process. Real-time, high-precision detection and control of melt pool characteristics serve as an effective method for enhancing the quality of cladding.

Compared with traditional laser cladding quality prediction methods [6], [7], [8], machine vision technology, as a non-contact and high-precision image processing technology, can detect the molten pool state in real time [9], [10]. Numerous researchers globally have begun to study the melt pool based on machine vision technology [11], [12]. Sun et al. [13] delved into the intricacies of the melt pool image processing

procedure and employed ellipse fitting to forecast the width and length characteristics of the melt pool. They achieved a prediction accuracy of 95% for width and 90% for length. Liu et al. [14] designed a coaxial CCD vision acquisition system. Aiming to solve the problem of the melt pool edge being difficult to extract due to the interference of liquid droplets and splashes, an edge extraction method based on phase consistency is proposed. Moreover, a multi-camera vision inspection approach was implemented to enhance the richness of deposition information. Huang et al. [15] established a binocular vision system utilizing GMAW to extract melt pool width using the minimum outer rectangle method. Yang et al. [16] devised a feedback controller based on this width measurement, significantly enhancing dimensional accuracy for curved, thin-walled components post-control implementation. Gu et al. [17] introduced an image-matching algorithm based on binocular vision technology, leveraging extracted feature point coordinates, colors, and other cues to enhance the precision of the 3D reconstruction of the melt pool. However, the reconstruction accuracy fell short of the requirements for practical application in production settings.

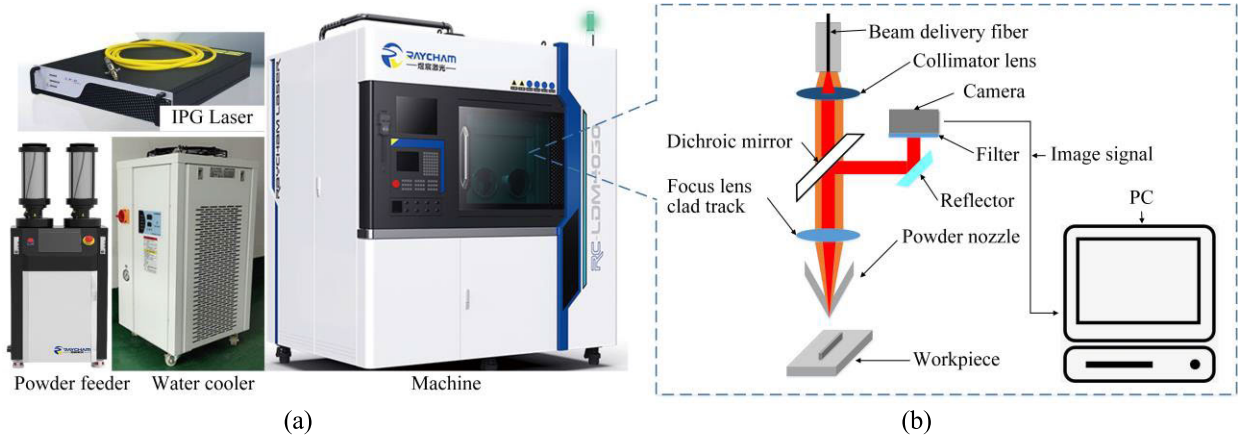The associate editor coordinating the review of this manuscript and approving it for publication was Jingang Jiang.

FIGURE 1. Experimental system: (a) Metal deposition equipment; (b) Detection principle.

In contrast to conventional approaches, machine vision-driven feature detection techniques offer enhanced detection consistency and are well-suited for real-time evaluation and feedback control of laser cladding quality [18], [19]. Nevertheless, the quality of image acquisition is highly susceptible to the complexity of the laser cladding environment [20], [21].

Hence, it is imperative to investigate feature extraction methods for laser cladding melt pools with anti-interference capabilities. Key melt pool features encompass morphological and thermal characteristics, ranking the width feature among the most crucial aspects of melt pool morphology. To align with industrial requisites, this study meticulously considers the spatial distribution pattern of melt pool width features and the computational efficacy of image algorithms. Drawing on image morphological erosion, an online method for extracting melt pool width features is suggested, offering ideas for achieving precise, efficient, and resilient extraction of these critical features.

II. EXPERIMENTAL METHODS

The experimental setup is depicted in Figure 1, showcasing the implementation of a coaxial melt pool inspection system constructed around the Nanjing Zhongke Raycham LDM-4030 metal deposition equipment. In Figure 1(a), the LDM-4030 metal deposition equipment is featured, comprising a Siemens-420D numerical control system, an IPG laser, an annular powder feeding head, and a water-cooling system. Figure 1(b) shows the coaxial vision melt pool detection principle. When operating, the laser emits a beam with a wavelength of 1070 nm through the forward optical path of the deposition head, focusing on the upper surface of the substrate. The spot diameter of the substrate surface is about 1.2 mm. The powder is melted at high temperature to form a melt pool, which emits "reflected light", which is incident on the CMOS camera through a beam splitter and a reflector. The front of the camera is equipped with a filter module, including a 540 nm bandpass filter and a 5% attenuator, which are used

TABLE 1. Chemical composition of Fe101 powder (weight percent).

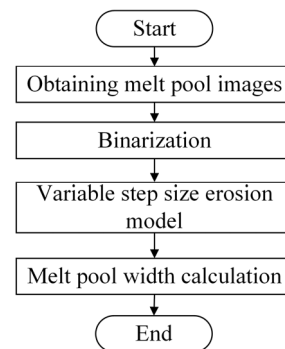| C	Mn	Si	Ni	Mo	Cr	N	P	Fe
0.03	0.35	7.86	0.77	14.55	0.12	0.045	0.42	Bal.

FIGURE 2. Melt pool feature extraction process.

to improve the clarity of the melt pool image and to prevent the incident light from exceeding the dynamic acquisition range of the camera, respectively.

In the course of the experiment, we observed that the melt pool section within the entire image was relatively minor. Employing ROI region segmentation aided in enhancing image detection accuracy and processing efficiency. Following segmentation, the image resolution was downscaled from 1024×768 to 200×192. Fe101 powder, characterized by a particle size range of 20 μm - 53 μm and chemical composition outlined in Table 1, was utilized for the experiment. The substrate material utilized was 316L, with dimensions of 100 mm $\times$ 100 mm $\times$ 20 mm, and the substrate surface was polished to remove burrs.

III. MODELING AND ANALYSIS

The extraction of melt pool width information necessitates a series of image processing steps, with the proposed melt pool width feature extraction process outlined in Figure 2.
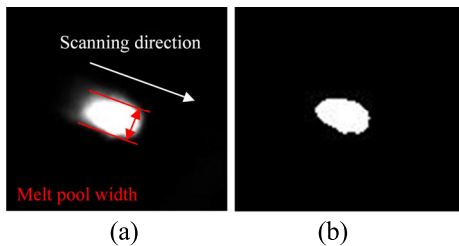
FIGURE 3. Image preprocessing: (a) Original image; (b) Preprocessed melt pool image.

A. IMAGE PREPROCESSING

Figure 3(a) depicts the initial melt pool image captured with the mentioned hardware setup. First, the melt pool image is processed morphologically, including converting the image to grayscale and applying median filtering. Graying diminishes the data channel, enhancing computational efficiency, while median filtering minimizes random noise interference in data transmission. Subsequently, the image is subjected to thresholding for segmentation purposes, with the adaptive and artificial thresholding methods being commonly employed techniques. In this study, artificial thresholding is employed to ascertain the threshold value, as this method is more effective in mitigating the impact of arc light. The first step is to conduct a single-track deposition experiment and simultaneously record the deposition track image. Then, microscopic data on the deposition track width section are extracted, and the average width from multiple data points is determined as the average deposition track width. This average width is then compared with the melt pool image width at various thresholds, and the threshold value is noted when the extracted image value aligns with the physical data. The threshold value of 90 was determined through repeated experiments, as illustrated in Figure 3(b). It is evident that the preprocessed melt pool image closely matches the original image, indicating the effectiveness of the threshold value selection process.

B. MODELING AND FEATURE EXTRACTION
1) MELT POOL WIDTH EXTRACTION

In the deposition process, the shape of the melt pool is primarily influenced by the laser spot, with the ideal shape being circular. However, variations in cooling rates between the front and end of the melt pool often result in a trailing tail at the end, causing the theoretical circle to transform into an ellipse. Analyzing the melt pool size characteristics and spatial distribution, we observed that the trailing tail enhances the melt pool length and area without considerable impact on the width. Moreover, considering the temperature analysis of the melted powder section, the highest temperature corresponds to the theoretical maximum diameter position of the melt pool. Given these physical laws, the study proposes a novel approach for feature extraction using the largest tangent circle diameter of the melt pool boundary as the melt pool width. This strategy ensures a comprehensive representation
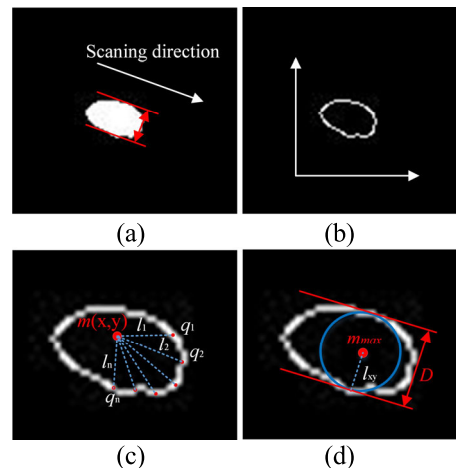

FIGURE 4. Melt pool width extraction process: (a) Preprocessed melt pool image; (b) Canny edge extraction; (c) Iterative process of the algorithm; (d) Extracted melt width.

of the melt pool geometry while accounting for variations caused by cooling rates and trailing tails.

In the melt pool width feature extraction process, the melt pool contour is an irregular convex packet. At this point, the problem of extracting melt pool width can be transformed into the traditional problem of extracting the maximum inscribed circle from an irregular convex packet. Figure 4 illustrates the results of applying the traditional tangent circle algorithm to extract the melt width from the melt pool image. The unit of measurement is in pixels, and the actual width of the melt pool can be obtained by multiplying the number of pixels by the calibration value. Traditional computational methods require contour extraction based on the pre-processed melt pool image. This paper uses the Canny algorithm, and the results are shown in Figure 4(b). Given a point $m(x, y)$ in the melt pool image and a set of contour points $q[q_1, q_2, \ldots, q_n]$ as shown in Figure 4(c), the computational model is then calculated as:

Step 1: Point $m(x, y)$ traverses the image from left to right and from top to bottom. Judge whether point $m(x, y)$ is within the contour boundary according to the coordinates of the contour points. If it is, keep it; otherwise, continue traversing.

Step 2: Calculate the minimum distance from $m(x, y)$ to the edge point $q[q_1, q_2, \ldots, q_n]$, denoted as $l[l_1, l_2, \ldots, l_n]$, find the minimum value $l(x, y)$ in the l as in (1).

$$l(x, y) = \min(l_1, l_2, l_3, \ldots, l_n) \qquad (1)$$

Step 3: Using point $m(x, y)$ as the circle center, and $l(x, y)$ as the radius, calculate area of the circle, denoted as S. Repeat steps 1 and 2, calculate all $S_{x,y}$ values as (2).

$$S_{\max} = \begin{cases} S_{x,y} & (S_{\max} < S_{x,y}) \\ S_{\max} & (S_{\max} \geq S_{x,y}) \end{cases} \qquad (2)$$
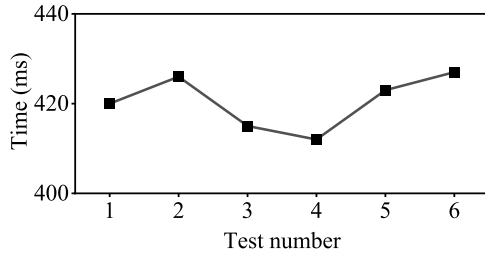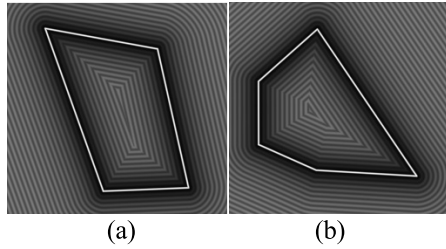
FIGURE 5. Algorithm runtime.

FIGURE 6. Image erosion process: (a) Quadrilateral; (b) Pentagon.

FIGURE 7. Erosion principle: (a) Binary image; (b) 3 × 3 convolution kernel; (c) Iteration result.

where S_{max} is the historical maximum value and $S_{x,y}$ is the current value.

Step 4: Find the distance l_{xy} corresponding to the area S_{max}, l_{xy} is the radius of the tangent circle, and the diameter of the tangent circle D is the width of the melt pool.

$$D = 2l_{xy} \quad (3)$$

Figure 5 illustrates the algorithm cycle time. The cycle is repeated 5 times for each image to prevent systematic errors, with an average time consumption of 420.5 ms. From the calculation process outlined in steps 1 to 4, it is evident that the traditional method requires iterating through all the pixel points in the image within the loop process and comparing the calculated results. The high number of iterations results in a time-consuming and redundant algorithm, falling short of meeting real-time feedback requirements. In response to this issue, this study introduces a variable step size erosion model.

2) VARIABLE STEP SIZE EROSION MODELING

The concept of erosion in imaging inspires the variable step size erosion model, as shown in Figure 6. The image is discretized into pixel points in image processing, and the contour can be approximated as a convex polygon. This polygon shrinks inward equidistantly in the direction normal to the edge of the polygon, eventually forming a triangle. The center of the inscribed circle of this triangle coincides with the center of the largest tangent circle of the polygon, and the minimum distance from this center to the contour of the melt pool represents the radius of the largest tangent circle of the melt pool. Each side of the polygon contracts by an equal distance, with the contraction endpoint becoming the center of the circle.
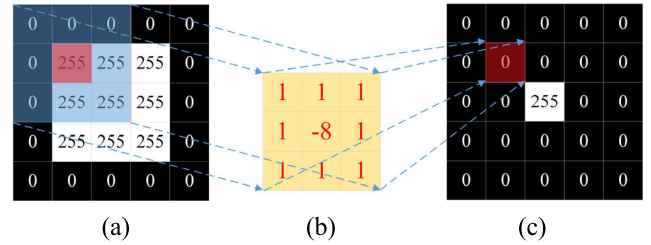
The contour contraction procedure is the convolution process in image processing. First, set the convolution kernel and set the target pixel coordinates as $f(x, y)$, with a 3×3 convolution kernel as (4):

$$\begin{bmatrix} x-1, y-1 & x, y-1 & x+1, y-1 \\ x-1, y & x,y & x+1, y \\ x-1, y+1 & x, y+1 & x+1, y+1 \end{bmatrix} \quad (4)$$

After that, the convolution operation is performed on the binary-valued melt pool image using a convolution kernel, where the target pixel is equal to the sum of the target region and the numerical multiplier of the convolution kernel, and the convolution law is given in (5):

$$f(x, y) = \begin{cases} 0(f(x, y) > 0) \\ 255(f(x, y) = 0) \\ 0(f(x, y) < 0) \end{cases} \quad (5)$$

Figure 7 shows the schematic diagram of the convolution principle. The binary map in Figure 7(a) is convolved according to the convolution law (5), iterating from left to right and top to bottom. The result of one convolution iteration is displayed in Figure 7(c).

Figure 8 shows the melt pool width feature extraction results with the erosion model applied to the case image. The preprocessed melt pool image can calculate the width after convolutional iteration, and the case image is iterated nine times. The result of running time consumption six times is shown in Figure 9, and the average time consumption is 14.7 ms, which is about 1/29 of the traditional detection algorithm and dramatically reduces the computation time consumption. As can be seen from the principle of the algorithm, each iteration of the convolution kernel will traverse the entire image. Hence, the size of the convolution kernel and the initial convolution position are two key factors that affect the speed of image feature extraction. In order to further improve the detection efficiency, an improved variable step size erosion method is proposed. The calculation steps are as follows:

Step 1: A point is randomly selected within the melt pool contour, and the shortest distance d from this point to each edge of the polygon is calculated.

Step 2: Parallel inward contraction of each side of the polygon, the distance between the parallel lines is d.
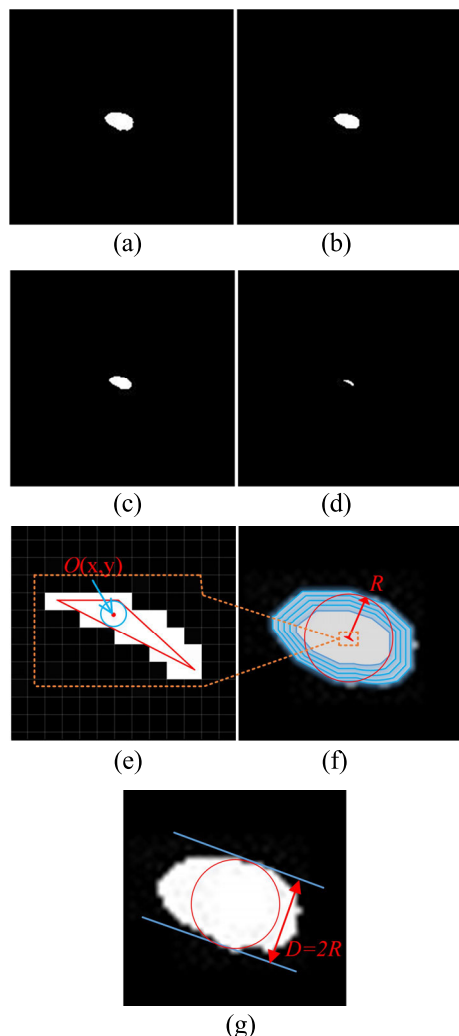
FIGURE 8. 3 × 3 Convolutional kernel convolutional process and results: (a) Original image; (b) 1st iteration; (c) 2nd iteration; (d) 9th iteration; (e) 9 iterations local enlarged image; (f) Schematic of edges for multiple iterations; (g) Melt pool width extraction results.
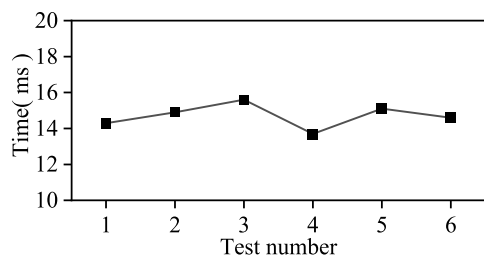

FIGURE 9. Algorithm runtime.

Step 3: Taking the focal point of the connecting line in step 2, a contour can be formed after shrinking one turn based on the original polygon.

Step 4: If the polygon generated in step 3 is a triangle, then calculate the tangent circle of the triangle; otherwise, repeat steps 1, 2, and 3 for the newly generated polygon.
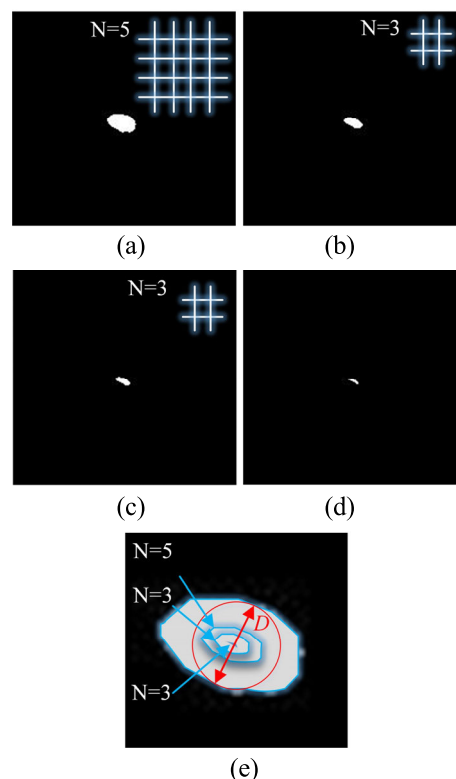

FIGURE 10. Variable step size convolution results: (a) Preprocessed melt pool image; (b) 1st iteration result; (c) 2nd iteration result; (d) Final convolution result; (e) Iteration process with tolerance width extraction.

The computational performance of the proposed algorithm is further optimized by introducing the variable step size model. The results are shown in Figures 10 and 11, Figure 10(a), (b), and (c) correspond to the generated convolution kernels of 5 × 5, 3 × 3, and 3 × 3. After the improvement, the number of algorithmic iterations is reduced from 9 to 3, and the average value of algorithmic time consumed is reduced from 14.7 ms to 3.2 ms. Commonly used digital communication methods in the industry, such as Modbus TCP, RS-232, and others, typically have a single communication time ranging from 10 ms to 20 ms. To ensure the software achieves the maximum communication frequency, it is essential to control the time consumption of the image data processing component within the single communication length as much as possible. Due to the variability in the convolutional kernel's size, the optimized algorithm's time-consuming stability decreases slightly but remains below 6 ms. This meets industrial requirements while also allowing for a particular execution space for data processing and transmission in other parts of the software.

C. COMPARISON OF EXTRACTION EFFECT OF MELT POOL WIDTH BY DIFFERENT METHODS

Its accuracy, efficiency, and anti-interference ability were tested to demonstrate the algorithm's advantages. Comparative experiments were conducted on several melt pool width
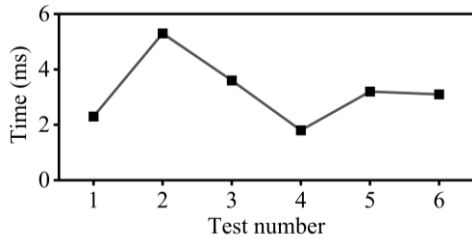
FIGURE 11. Algorithm runtime.

extraction algorithms. The melt pool coaxial vision acquisition software was jointly developed based on C++ and QT platforms. The software runs on a Windows 10 system with GPU model i5-1135, 16GB of RAM, and a central frequency of 2.4GHz.

The sampling method is illustrated in Figure 12, and the single-track deposition experiment is conducted initially. In the single-track deposition of laser cladding, overlap rate, and interlayer lift height are not involved, making it more convenient for metallographic observation. The experimental parameters included a power of 600 W, scanning speed of 10 mm/s, and powder feeding rate of 1.6 g/s. Figure 12(a) displays the morphology of the deposited single track, and Figure 12(b) presents the 2D melt pool image captured by the coaxial vision system. Interferences such as powder splash, melt droplets, and arc light during the deposition process significantly impact the robustness of melt pool feature detection. Hence, three interferences with low, medium, and high levels were manually chosen to test the algorithm's robustness. Following the selection of interference groups of melt pool images, the deposition locations of the melt pool images can be determined by calculating based on the corresponding timestamps of each image in the video captured by the system, as indicated by the labeling in Figure 12(a). The actual melt pool width value can be obtained through sectional microscopic measurements at the labeled positions. A schematic diagram of the metallographic measurement of the melt pool width is shown in Figure 12(c).

Melt pool feature prediction methods can be divided into traditional image processing algorithms and machine learning-based methods that have been gradually developed in recent years [22], [23], [24]. The machine learning method requires high labeling accuracy and a large volume of data, leading to poor real-time performance. It is mainly in the experimental stage, and no commercial applications have been identified yet. Therefore, traditional image detection algorithms remain the preferred technical approach. In this paper, three algorithms - the minimum external rectangle (MER) algorithm [15], [16], the ellipse fitting (EF) algorithm [13], and the boundary intersection (BI) algorithm [25] - are selected for comparison. The MER algorithm utilizes the short side of the minimum external rectangle of the melt pool contour as the width of the melt pool. The EF algorithm considers the short axis dimension of the smallest external ellipse of the contour as the width
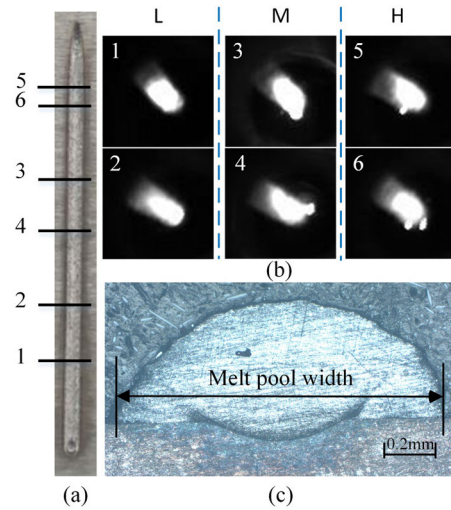

FIGURE 12. The process of sampling the melt pool width: (a) Single-track deposition morphology; (b) Melt pool two-dimensional image; (c) Melt pool metallographic image.

TABLE 2. Actual and predicted values (unit: pixel).

Interference level	Measured value	MER	EF	BI	Proposed
L.1	15.4	16.6	17.4	17.6	15.9
L.2	15.0	15.8	16.1	16.3	15.5
M.1	15.4	17.7	19.5	18.9	15.9
M.2	15.5	18.1	19.3	20.7	15.8
H.1	14.2	17.3	18.3	19.5	14.5
H.2	14.7	17.8	18.1	18.4	15.2

of the melt pool. In the BI algorithm, the average vector in the direction of scanning speed is first calculated. Then, the distance between the average vector and the two intersections of the melt pool contour is calculated as the width of the melt pool. Figures 13 to 15 display the results of melt pool width extraction under various interference conditions. Table 2 presents the corresponding detection data. Figure 16 illustrates the four algorithms' melt width extraction error and running time consumption results. It is evident that under low interference, all four algorithms demonstrate high accuracy with an error of less than 3 pixels. As the interference increases, the recognition errors of the three algorithms in the comparison group appear to increase to varying degrees. Among them, the BI algorithm exhibits the most significant error, particularly under high interference conditions, with a maximum error value of 5.2 pixels. This is because when random disturbances, such as powder splash, arc light, etc., appear near the normal vector and the boundary point, the interferences will be directly introduced into the calculation results, causing the error to increase. This also indicates that the robustness of the algorithm is poor.

Figure 16(b) shows that the accuracy of the MER algorithm and the EF algorithm is moderate. However, in conjunction with Figures 13 to 15, we observed that using the short side
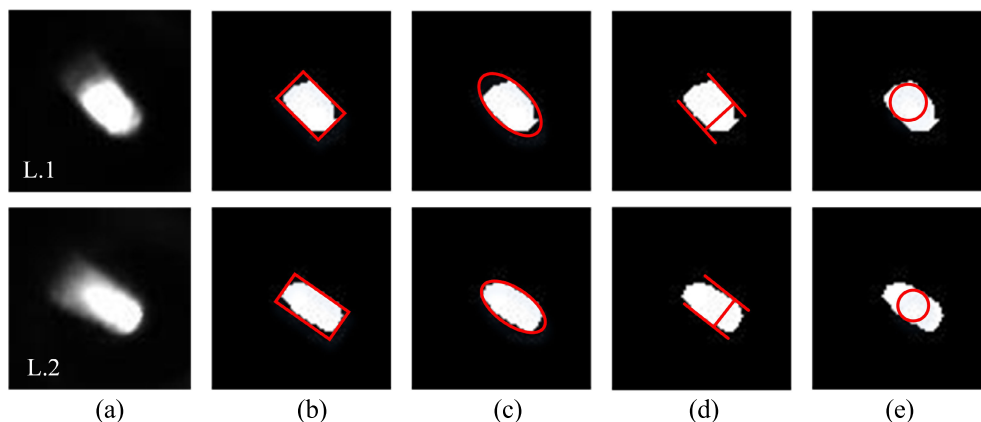
FIGURE 13. Comparison results of algorithms under low perturbation: (a) Original image; (b) MER algorithm; (c) EF algorithm; (d) BI algorithm; (e) Algorithm in this paper.
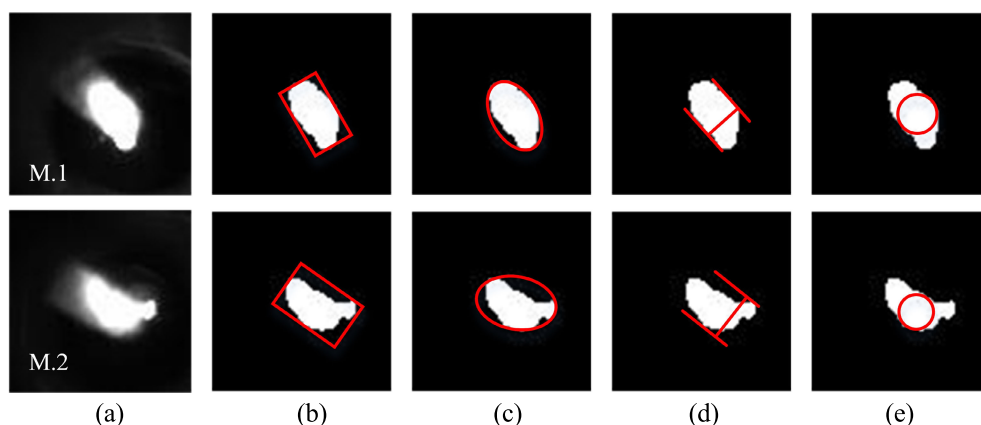

FIGURE 14. Comparison results of algorithms under medium perturbation: (a) Original image; (b) MER algorithm; (c) EF algorithm; (d) BI algorithm; (e) Algorithm in this paper.
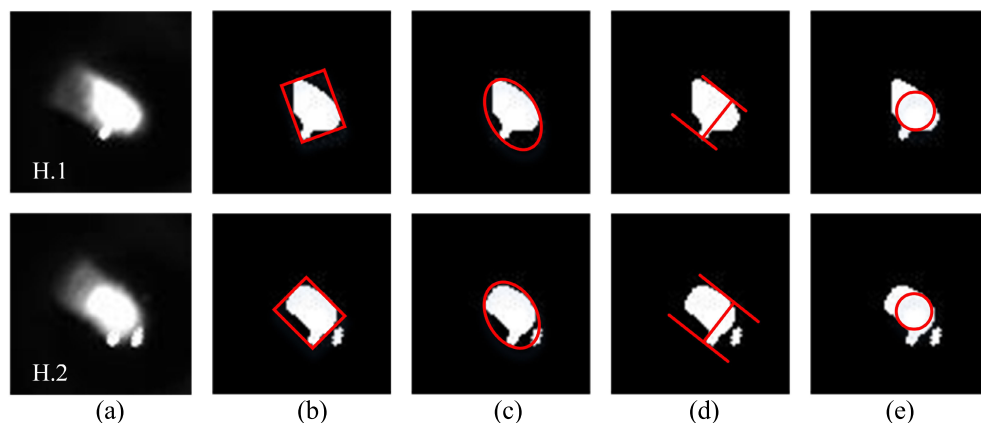

FIGURE 15. Comparison results of algorithms under higher perturbation: (a) Original image; (b) MER algorithm; (c) EF algorithm; (d) BI algorithm; (e) Algorithm in this paper.

of the melt pool contour's minimum external rectangle as the melt pool width will lead to a situation where the short side does not coincide with the direction of the melt pool width. Similarly, this problem also arises in the EF algorithm. The direction of the melt pool width is theoretically perpendicular to the direction of the scanning speed of the deposition head. When the directions do not match, the detection results are not accurate. Although the BI algorithm guarantees direction consistency, the robustness is insufficient. At the same time, the algorithm proposed in this study exhibits the optimal
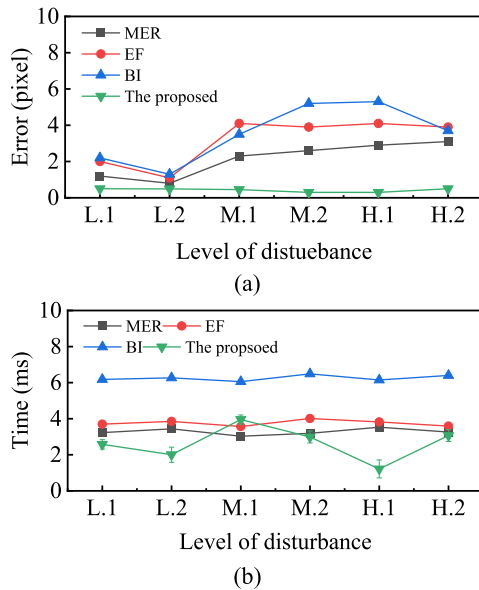
FIGURE 16. Comparison of the results of the four algorithms: (a) Error; (b) Time consuming.

detection accuracy under various interference levels, with an average detection error of less than 1 pixel. The algorithm thoroughly considers the spatial location characteristics of the melt pool width features, enhancing robustness and effectively bypassing the problem of directional inconsistency between the detected and actual features. In terms of computational efficiency, all four algorithms meet the requirements of industrial applications. The MER and EF algorithms have similar computational ideas and need to conduct iterative computations based on the melt pool contour point information, taking around 3 ms to 4 ms. The BI algorithm requires the judgment and calculation of direction vectors and contour calculation, making it the most time-consuming, at approximately 6 ms. The variable step-size erosion model proposed in this study significantly enhances computational efficiency, enabling the algorithm to be industrially deployed with a runtime of 1 ms to 4 ms. The computational time-consuming fluctuation of this algorithm is slightly insufficient compared to the other three algorithms, which can serve as a direction for optimizing subsequent algorithms.

In addition to the points mentioned above, during testing in an industrial application environment, we discovered that camera exposure significantly affects the detection of the melt pool width. In the initial stages of this work, Fe101 powder was used for targeted testing, and manual exposure control led to high detection accuracy. However, in industrial applications, the reflective properties of various powders vary significantly. Therefore, developing adaptive exposure technology or establishing a process-matching library is another focus area that the algorithm will address in the future.

IV. CONCLUSION
1) Interferences such as powder splashing and arc light generated during the laser deposition process can sig-

nificantly affect the accuracy of extracting melt pool width features.
2) The variable step-size erosion model proposed in this study fully considers the spatial distribution characteristics of melt pool width features. Experimental results demonstrate that the method has good extraction accuracy, efficiency, and robustness, meeting the requirements for industrial applications.

REFERENCES

[1] L. Qin, K. Wang, X. Li, S. Zhou, and G. Yang, "Review of the formation mechanisms and control methods of geometrical defects in laser deposition manufacturing," *Chin. J. Mech. Eng., Additive Manuf. Frontiers*, vol. 1, no. 4, Dec. 2022, Art. no. 100052.

[2] T. Herzog, M. Brandt, A. Trinchi, A. Sola, and A. Molotnikov, "Process monitoring and machine learning for defect detection in laser-based metal additive manufacturing," *J. Intell. Manuf.*, vol. 35, no. 4, pp. 1407–1437, Apr. 2024.

[3] A. Shrivastava, S. Mukherjee, and S. S. Chakraborty, "Addressing the challenges in remanufacturing by laser-based material deposition techniques," *Opt. Laser Technol.*, vol. 144, Dec. 2021, Art. no. 107404.

[4] X. Lin, K. Zhu, J. Y. H. Fuh, and X. Duan, "Metal-based additive manufacturing condition monitoring methods: From measurement to control," *ISA Trans.*, vol. 120, pp. 147–166, Jan. 2022.

[5] R. McCann, M. A. Obeidi, C. Hughes, É. McCarthy, D. S. Egan, R. K. Vijayaraghavan, A. M. Joshi, V. Acinas Garzon, D. P. Dowling, P. J. McNally, and D. Brabazon, "In-situ sensing, process monitoring and machine control in laser powder bed fusion: A review," *Additive Manuf.*, vol. 45, Sep. 2021, Art. no. 102058.

[6] Y. Li, H. Mu, J. Polden, H. Li, L. Wang, C. Xia, and Z. Pan, "Towards intelligent monitoring system in wire arc additive manufacturing: A surface anomaly detector on a small dataset," *Int. J. Adv. Manuf. Technol.*, vol. 120, nos. 7–8, pp. 5225–5242, Jun. 2022.

[7] L. Zhu, P. Xue, Q. Lan, G. Meng, Y. Ren, Z. Yang, P. Xu, and Z. Liu, "Recent research and development status of laser cladding: A review," *Opt. Laser Technol.*, vol. 138, Jun. 2021, Art. no. 106915.

[8] M. Cheng, Y. Wu, Z. Zhao, G. Luo, L. Song, and W. Xiao, "Texture tailored through combination of molten pool morphology and scanning path in laser additive manufacturing of Alloy 718," *Mater. Today Commun.*, vol. 39, Jun. 2024, Art. no. 108885.

[9] Z.-J. Tang, W.-W. Liu, Y.-W. Wang, K. M. Saleheen, Z.-C. Liu, S.-T. Peng, Z. Zhang, and H.-C. Zhang, "A review on in situ monitoring technology for directed energy deposition of metals," *Int. J. Adv. Manuf. Technol.*, vol. 108, nos. 11–12, pp. 3437–3463, Jun. 2020.

[10] C. Tan, R. Li, J. Su, D. Du, Y. Du, B. Attard, and A. Dong, "Review on field assisted metal additive manufacturing," *Int. J. Mach. Tools Manuf.*, vol. 189, Jun. 2023, Art. no. 104032.

[11] Z. Zhao, B. Sun, Y. Zhang, L. Bai, and J. Han, "Weld pool image acquisition and contour extraction based on arc spectrum and camera quantum efficiency," *Optik*, vol. 202, Feb. 2020, Art. no. 163719.

[12] Z.-J. Tang, W.-W. Liu, N. Zhang, Y.-W. Wang, and H.-C. Zhang, "Real–time prediction of penetration depths of laser surface melting based on coaxial visual monitoring," *Opt. Lasers Eng.*, vol. 128, May 2020, Art. no. 106034.

[13] Z. Sun, W. Guo, and L. Li, "In-process measurement of melt pool cross-sectional geometry and grain orientation in a laser directed energy deposition additive manufacturing process," *Opt. Laser Technol.*, vol. 129, Sep. 2020, Art. no. 106280.

[14] J. Liu, "New method based on phase congruency for weld pool edge extraction in laser cladding," *J. Mech. Eng.*, vol. 54, no. 5, p. 166, 2018.

[15] H. Junfen, X. Long, H. Jiqiang, Z. Yong, M. Ke, and J. Xiangdong, "GMAW penetration state prediction based on visual sensing," *J. Mech. Eng.*, vol. 55, no. 17, p. 41, 2019.

[16] Q. Yang, Z. Yuan, X. Zhi, Z. Yan, H. Tian, and X. Chen, "Real-time width control of molten pool in laser engineered net shaping based on dual-color image," *Opt. Laser Technol.*, vol. 123, Mar. 2020, Art. no. 105925.

[17] Z. Gu, J. Chen, and C. Wu, "Three-dimensional reconstruction of welding pool surface by binocular vision," *Chin. J. Mech. Eng.*, vol. 34, no. 1, May 2021, Art. no. 47.

[18] P. Colodrón, J. Fariña, J. J. Rodríguez-Andina, F. Vidal, J. L. Mato, and M. Á. Montealegre, "FPGA-based measurement of melt pool size in laser cladding systems," in *Proc. IEEE Int. Symp. Ind. Electron.*, Jun. 2011, pp. 1503–1508.

[19] L. Zheng, Q. Zhang, H. Cao, W. Wu, H. Ma, X. Ding, J. Yang, X. Duan, and S. Fan, "Melt pool boundary extraction and its width prediction from infrared images in selective laser melting," *Mater. Design*, vol. 183, Dec. 2019, Art. no. 108110.

[20] R. Sampson, R. Lancaster, M. Sutcliffe, D. Carswell, C. Hauser, and J. Barras, "An improved methodology of melt pool monitoring of direct energy deposition processes," *Opt. Laser Technol.*, vol. 127, Jul. 2020, Art. no. 106194.

[21] W. Huang and R. Kovacevic, "Development of a real-time laser-based machine vision system to monitor and control welding processes," *Int. J. Adv. Manuf. Technol.*, vol. 63, nos. 1–4, pp. 235–248, Nov. 2012.

[22] I. Jeon, L. Yang, K. Ryu, and H. Sohn, "Online melt pool depth estimation during directed energy deposition using coaxial infrared camera, laser line scanner, and artificial neural network," *Additive Manuf.*, vol. 47, Nov. 2021, Art. no. 102295.

[23] Q. Zhu, Z. Liu, and J. Yan, "Machine learning for metal additive manufacturing: Predicting temperature and melt pool fluid dynamics using physics-informed neural networks," *Comput. Mech.*, vol. 67, no. 2, pp. 619–635, Feb. 2021.

[24] Z. Zhang, C. K. Sahu, S. K. Singh, R. Rai, Z. Yang, and Y. Lu, "Machine learning based prediction of melt pool morphology in a laser-based powder bed fusion additive manufacturing process," *Int. J. Prod. Res.*, vol. 62, no. 5, pp. 1803–1817, Apr. 2023.

[25] Y. Su, Z. Wang, X. Xu, K. Luo, and J. Lu, "Effect of closed-loop controlled melt pool width on microstructure and tensile property for Fe-Ni-Cr alloy in directed energy deposition," *J. Manuf. Processes*, vol. 82, pp. 708–721, Oct. 2022.

LIGUO MIAO received the B.Eng. and M.Sc. degrees in mechanical engineering from Shenyang University of Technology (SUT), Shenyang, China, in 2016 and 2019, respectively, where he is currently pursuing the Ph.D. degree in mechanical engineering. His current research interests include additive manufacturing quality monitoring, microphysical characterization, and evaluation of metallic materials.

JINGHU TANG received the M.Sc. degree in mechanical engineering from Shenyang University of Technology (SUT), Shenyang, China, in 2019. He is currently pursuing the Ph.D. degree in mechanical engineering with Northeastern University (NEU), Shenyang. His current research interests include process equipment design development, structure optimization, and precision machinery design and manufacturing.
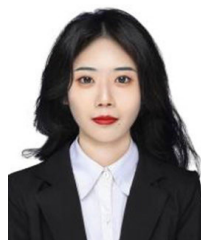
YUANXIN CHAI received the B.Eng. and M.Sc. degrees in mechanical engineering from Liaoning University of Technology (LUT), Jinzhou, China, in 2017 and 2020, respectively. She is currently pursuing the Ph.D. degree in mechanical engineering with Shenyang University of Technology (SUT), Shenyang, China. Her current research interests include additive manufacturing process optimization and process simulation, microstructure analysis, and residual stress characterization of metallic materials.
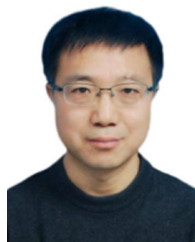
DIANQI LI received the M.Sc. degree in solid mechanics and the Ph.D. degree in pattern recognition and intelligent systems from Northeastern University (NEU), Shenyang, China, in 2002 and 2007, respectively. He is currently a Ph.D. Advisor with Shenyang University of Technology (SUT), Shenyang. His current research interests include failure analysis and prediction of metallic materials under special service conditions, tissue modulation of metal matrix composites, and material preparation.

• • •